Alexandria Engineering Journal 86 (2024) 346–359

Contents lists available at ScienceDirect

Alexandria Engineering Journal

journal homepage: www.elsevier.com/locate/aej

# The influence of aspect ratios of two elliptical cylinders on the solid-liquid phase change flow

Nidhal Ben Khedher [a,b], Maryam Ghodrat [c], Mikhail Sheremet [d], Amira M. Hussin [e], Mohamed Houcine Dhaou [f], S.A.M. Mehryan [g,*], Mohsen Sharifpur [h,i,**]

[a] Department of Mechanical Engineering, College of Engineering, University of Ha'il, P.O. Box 2440, Ha'il City, Saudi Arabia
[b] Laboratory of Thermal and Energetic Systems Studies (LESTE) at the National School of Engineering of Monastir, University of Monastir, 5000, Tunisia
[c] School of Engineering and Technology, University of New South Wales Canberra, Canberra 2610, ACT, Australia
[d] Laboratory on Convective Heat and Mass Transfer, Tomsk State University, 634050, Tomsk, Russia
[e] Department of Mathematics, Al-Aflaj College of Science and Humanities, Prince Sattam bin Abdulaziz, University, Al-Aflaj 710-11912, Saudi Arabia
[f] Department of Physics, College of Science, Qassim University, P.O.Box, 6644, Buraydah Almolaydah 51452, Saudi Arabia
[g] Young Researchers and Elite Club, Yasooj Branch, Islamic Azad University, Yasooj, Iran
[h] Department of Mechanical and Aeronautical Engineering, University of Pretoria, 0028, South Africa
[i] Department of Medical Research, China Medical University Hospital, China Medical University, Taichung 404, Taiwan

ARTICLE INFO

*Keywords:*
Phase change material
Heat storage
Elliptical chargers
Simulation
Thermal energy

ABSTRACT

Nowadays, phase change materials are widespread in different engineering applications including cooling of electronics, thermal performance in building elements, heat exchangers, and many more. It is critical to gain thorough comprehension on phase change material behavior. The present research aims to numerically simulate phase change material in a heat storage unit having two isothermal elliptical elements. The formulated partial differential equations have been solved by the finite element technique taking into account the enthalpy-porosity approach and adaptive mesh refinement technique. The developed computational code has been validated using numerical and experimental data from the literature. The influence of the aspect ratios of the two elliptical cylinders on the melting phenomenon has been scrutinized, and the most efficient shapes have been identified. It has been found that more intensive melting occurs when the aspect ratios of the upper and lower cylinders are $AR_u = 0.25$ and $AR_l = 4.0$, with a reduction of 18.45 % in the melting time compared to the case with $AR_u = AR_l = 1.0$. Furthermore, the case with $AR_u = 1.0$ and $AR_l = 0.5$ shows the longest melting time, with an increase of 0.6 % in the melting time compared to the case with $AR_u = AR_l = 1.0$.

## 1. Introduction

Due to its importance in numerous applications such as battery lifespan, solar energy storage, refrigeration systems, thermal management of electronic devices, crystal growth, and metal casting, latent heat thermal energy storage (LHTES) units have attracted much attention in the literature. To store energy, these systems employ a variety of phase change materials (PCMs), including organic, inorganic, and salt eutectics. The prospective applications of PCMs in different energy storage units have been extensively investigated in several comprehensive studies published in the literature [1–7]. Huge specific heat values during the melting process allow PCMs to absorb large quantities of energy, and low specific heat values during solidification allow the stored energy to be released. In addition, PCMs are currently available in a wide range of working temperatures, making them more versatile [8–10].

Dukhan et al. [11] conducted an experiment investigating the charging process of a PCM within concentric annular cavities of both horizontal and vertical heat exchangers. The study showed that the charging rate is influenced by both the inlet water temperature and the orientation of the heat exchangers. Dhaidan [12] explored how the transient dynamics of the melting-front and liquid fraction are affected by two different capsule orientations: prolate and oblate. The findings demonstrated that the applied wall heat flux significantly affects the melting characteristics, with minimal impact observed on the melting process due to the orientation of the capsule. Despite this, the melting process occurs relatively faster, and less time is necessary in an oblate

* Corresponding author.
** Corresponding author at: Department of Mechanical and Aeronautical Engineering, University of Pretoria, 0028, South Africa.
*E-mail addresses:* alal171366244@gmail.com (S.A.M. Mehryan), mohsen.sharifpur@up.ac.za (M. Sharifpur).

https://doi.org/10.1016/j.aej.2023.11.048
Received 20 May 2023; Received in revised form 18 October 2023; Accepted 15 November 2023
Available online 2 December 2023

**Nomenclature**

*Latin symbols*

| | |
|---|---|
| $A$ | Surface area of PCM ($m^2$) |
| $A^*$ | Mushy zone parameter ($5 \times 10^5$) |
| $a_1$ | Radius of the lower ellipse along the $x$-axis |
| $a_2$ | Radius of the upper ellipse along the $x$-axis |
| $AR_l$ | Aspect ratio of the lower elliptical cylinder |
| $AR_u$ | Aspect ratio of the upper elliptical cylinder |
| $b_1$ | Radius of the lower ellipse along the $y$-axis |
| $b_2$ | Radius of the upper ellipse along the $y$-axis |
| $c_p$ | Sensible heat capacity ($Jkg^{-1}K^{-1}$) |
| $g$ | Gravity acceleration ($ms^{-2}$) |
| $h_{PCM}$ | Latent heat of PCM ($kJkg^{-1}$) |
| $k$ | Thermal conductivity ($Wm^{-1}K^{-1}$) |
| $L$ | Size of square enclosure ($m$) |
| $p$ | Pressure ($Pa$) |
| $q_i$ | $i$th component of the velocity vector ($ms^{-1}$) |
| $T$ | Temperature ($K$) |
| $t$ | Time ($s$) |
| $x, y$ | Cartesian coordinates ($m$) |

*Greek symbols*

| | |
|---|---|
| $\beta$ | Thermal expansion coefficient of liquid PCM ($K^{-1}$) |
| $\delta T_{mel}$ | Melting temperature window ($K$) |
| $\Omega(T)$ | Numerical step function |
| $\mu$ | Dynamic viscosity ($Nsm^{-2}$) |
| $\rho$ | Density ($kgm^{-3}$) |

*Subscripts*

| | |
|---|---|
| *initial* | Initial condition |
| *h* | Hot wall |
| *lPCM* | Liquid phase change material |
| *sPCM* | Solid phase change material |
| *mel* | Melting point |
| *PCM* | Phase change material |

*Abbreviations*

| | |
|---|---|
| *MVF* | Melted volume fraction |
| *PCM* | Phase change material |
| *PMTC* | Percentage of a decrease or increase in the melting time |

capsule compared to the duration experienced in the prolate capsule.

Huang et al. [13] devised and applied an innovative method for optimizing the morphology of PCM heat sinks. The initial step involved simulating the operational processes of the low melting point alloy-based PCM heat sink using a 2D numerical model. Next, morphological operations, involving erosion and dilation, were executed to revise the material distribution within the target domain, guided by the simulation outcomes. Through an iterative combination of simulations and morphological operations, the optimal enclosure shape was achieved, and the resulting optimization outcomes underwent additional experimental validation. The suggested optimization approach demonstrated its capability to achieve superior results compared to conventional methods. Mukhesh et al. [14] presented experimental and numerical explorations focusing on thermal convection near horizontal heat transfer fluid pathways—both straight and wavy—within a rectangular cavity containing phase change material. The findings revealed a strong concurrence between the finite volume simulations based on enthalpy-porosity and the experimental temperature responses, affirming the precision of the computational method.

Several numerical studies [15–20] investigated the melting of PCMs in various enclosure shapes, including annulus, ducting, triangular, and spherical shells. Al-Abidi et al. [15] used both commercial computational fluid dynamics (CFD) software and self-developed programming to perform a complete assessment of CFD applications for LHTES systems. They concluded that optimizing LHTES performance with CFD software was a viable option. Elsayed [18] conducted a numerical study to examine the characteristics of PCM melting within a triangular cylinder enclosure. The study used paraffin wax as a PCM, with a hot air stream acting as a heat source to melt the PCM. Three equal-volume triangular cylinders with varying apex angles were analyzed employing ANSYS-Fluent software. The apex angle and the triangle base length, according to the author [18], have a significant impact on the container surface temperature and heat storage efficiency.

Soodmand et al. [19] examined the thermal behavior of rectangular, triangular, and cylindrical chambers during the melting and solidification processes. The findings suggested that the horizontal rectangular and triangular cavities exhibit the fastest melting rates. Additionally, the results highlighted that the solidification liquid fraction for a cylindrical shape is higher compared to other shapes. Dhaidan et al. [20] investigated the melting process of paraffin within a hemicylindrical storage chamber using both numerical simulations and experimental methods. The results revealed that with an increase in chamber diameter from 200 to 400 mm, the melting time experiences a threefold increase at a wall temperature of 90 °C. Furthermore, the melting rate of the PCM within the hemicylindrical chamber surpassed that observed in a rectangular chamber of equal volume.

The presence of heated cylinders within the enclosure holds potential for diverse thermal applications, encompassing electronic devices, heat exchangers, solar installations, nuclear reactors, the thermal design of passive cooling systems, and more [21,22]. Hence, the use of PCM in vicinity of the heated cylinders could be considered as an approach for cooling and storing thermal energy. In these systems, the heat transfer rate and, consequently, the melting process are influenced by interactions among the surfaces of cylinders and between the cylinder surfaces and the enclosure walls. Therefore, it is crucial to ascertain the optimal shapes of heated cylinders, with the aim of achieving the highest level of thermal performance. Sasaguchi et al. [23] used a computational model to study the melting flow within a rectangular cavity having a single and two horizontal hot cylinders which were vertically spaced. When starting with an initial water temperature of 0 °C, their investigation revealed that the solidification process was slower for two cylinders compared to a single cylinder. The influence of a cylinder's vertical location on the phase change flow of water/ice around a horizontal cylinder in an enclosure was quantitatively explored by Sugawara et al. [22]. According to the authors, the melting rate falls dramatically as the cylinder distance from the bottom wall increases.

Using the finite-volume method, Mahdaoui et al. [24] quantitatively investigated the melting flow around a horizontal cylinder inside a cavity. In their study, the enclosed medium was saturated with pure gallium as the PCM. The authors found that the natural convection mechanism transfers the majority of energy from the higher to the lower region of the hot cylinder. Memon et al. [21] used a 2D heated cylinder inside a square cavity saturated with lauric acid as the PCM to examine laminar natural convection. They showed that the melt fraction decreased as the cylinder moved away from the base of the enclosure. The authors also demonstrated that altering the placement of the cylinder improved the melting and energy storage rates. Mishra et al. [25] used a numerical simulation to investigate the melting and heat transfer characteristics of a heated cylinder inside twelve variably shaped enclosures. The amount of PCM above the cylinder and the interaction between the insulated walls of the enclosure and the heated surface of the cylinder were discovered to have a significant impact on the melting

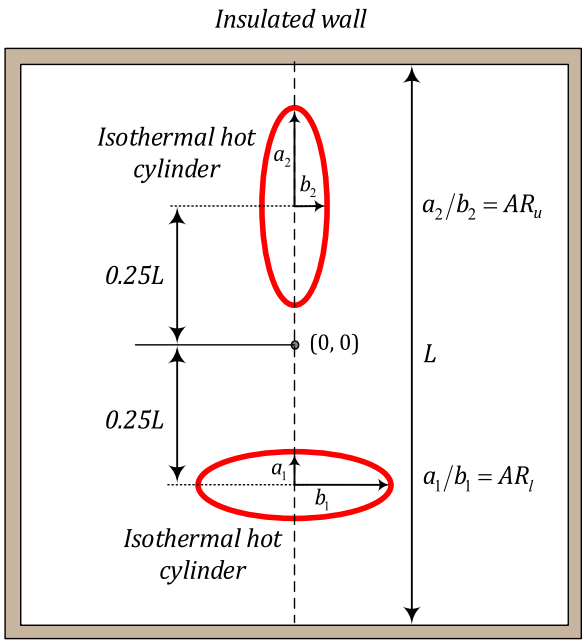


**Fig. 1.** Physical schematic of the problem.

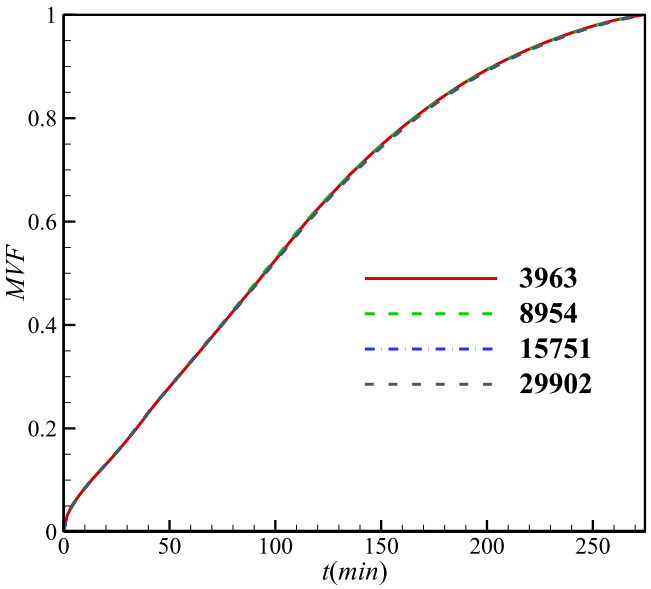


**Fig. 3.** Dependency of the *MVF* on the grid size.

rate. It was found that the inverted semi-circular chamber has the fastest melting rate.

A thorough review of the literature suggests that variations in the geometric morphologies of the inner cylinders within the enclosure filled with solid PCM still need to be investigated further. Although numerous studies have been conducted on the melting process in the presence of one or more circular cylinders within closed compartments, the literature review reveals that no study to date has delved into the effect of aspect ratios of two elliptical cylinders on the phase change flow in an enclosed medium. Hence, this research aims to investigate the impact of elliptical cylinders with varying aspect ratios on the melting

**Table 1**
Thermophysical specifications of the PCM [26].

| Thermal expansion coefficient (1/K) | Dynamic viscosity (mPa·s) | Density ($kg \cdot m^{-3}$) | | Thermal conductivity ($W \cdot m^{-1} \cdot K^{-1}$) | | Specific heat capacity ($kJ \cdot kg^{-1} \cdot K^{-1}$) | |
|---|---|---|---|---|---|---|---|
| | | solid | liquid | solid | liquid | solid | liquid |
| $1.018 \times 10^{-3}$ | 13.23 | 891.4 | 821.6 | 0.252 | 0.159 | 2040 | 2360 |

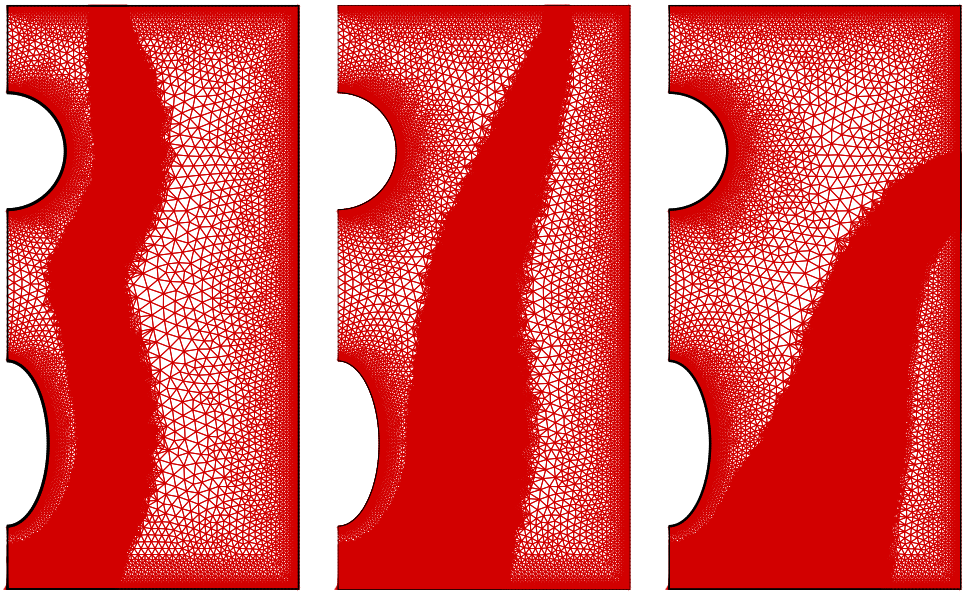


**Fig. 2.** Progressive adaptive mesh at different times.

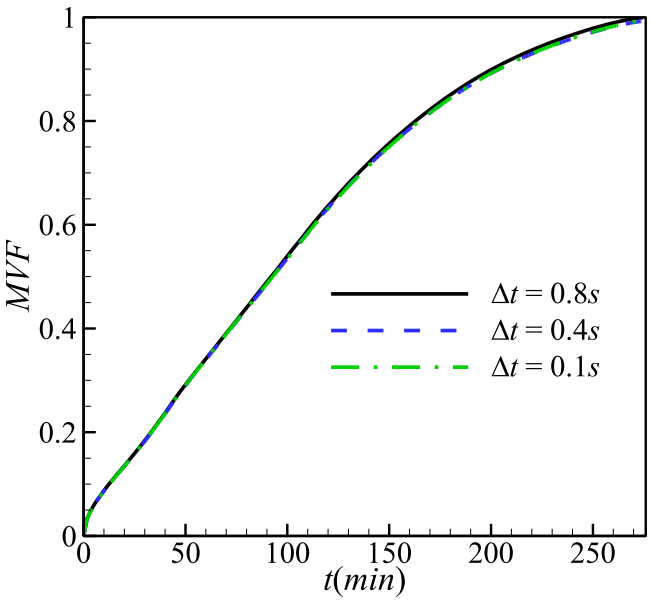


**Fig. 4.** Dependency of the *MVF* on the time step.

and heat transfer characteristics of a PCM inside an enclosure. This research also aims to explore numerically how variations in the aspect ratios of the cylinders inside the enclosure affect the melt volume fraction, streamlines, and isotherms. According to the aspect ratios of the lower ($AR_l$) and upper ($AR_u$) elliptical cylinders, 25 different cases are studied. It is worth noting that $AR_l$ and $AR_u$ vary from 0.25 to 4.0.

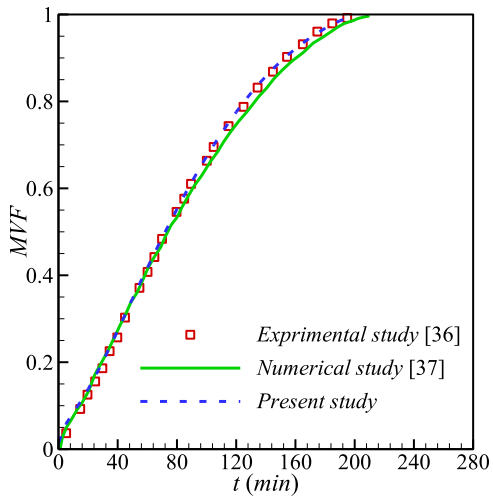


**Fig. 6.** Comparison of the *MVF* from the experimental and numerical studies conducted by Kamkari et al. [36,37] with that predicted by the present study.

## 2. Mathematical modeling

Fig. 1 displays the physical schematic of an enclosed medium having two elliptical cylinders, both maintained at a high temperature of $T_h$. However, the thermally insulated wall boundary condition is applied at the outer boundaries of the enclosure. The enclosure is filled with 1-Tetradecanol as the PCM. Table 1 presents the properties of the PCM. The melting temperature and latent heat of the PCM are 37 °C and 227.8 kJ/kg, respectively [26]. The size of the 2D square enclosure is 50 mm, and the aspect ratios of the lower and upper elliptical cylinders are $AR_l$ ($AR_l$

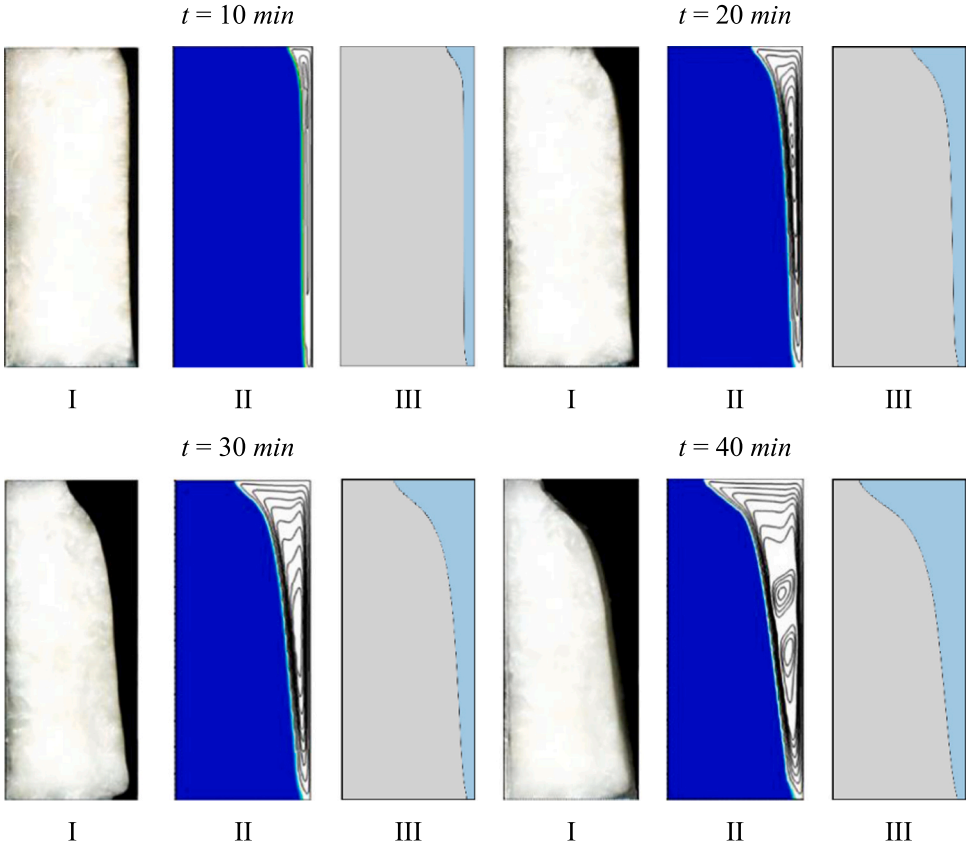


**Fig. 5.** Evaluation of the molten liquid fields of the current work through the experimental and numerical results reported in [36,37]; I) experimental results, II) numerical results, and III) current work.

**Table 2**
The studied cases number.

| $AR_l$ / $AR_u$ | 0.25 | 0.50 | 1.00 | 2.00 | 4.00 |
|---|---|---|---|---|---|
| 0.25 | C1 | C2 | C3 | C4 | C5 |
| 0.50 | C6 | C7 | C8 | C9 | C10 |
| 1.00 | C11 | C12 | C13 | C14 | C15 |
| 2.00 | C16 | C17 | C18 | C19 | C20 |
| 4.00 | C21 | C22 | C23 | C24 | C25 |

$= b_1/a_1$) and $AR_u$ ($AR_u = b_2/a_2$). It is worth noting that the surface area of the cylinders is identical and constant.

The following assumptions are employed for simulating the melting flow of the PCM:

I) The molten flow of PCM is Newtonian and laminar.
II) The volume change of PCM is neglected when transferring from the solid phase to the liquid phase.
III) The thermophysical properties of the solid and liquid phases are different, and remain constant for each respective phase throughout the heat transfer process.
IV) The molten fluid is incompressible with viscous dissipation effect being ignored.
V) The Boussinesq linear approximation is valid for modeling the variation of the PCM density in the buoyancy term.

The enthalpy-porosity scheme along with an adaptive mesh refinement is used to model progressive melting front. The balance equations of mass, momentum, and energy are listed below [27]:

$$\frac{\partial q_j}{\partial x_j} = 0 \tag{1}$$

where $x_1{}^\circ = {}^\circ x$ and $x_2{}^\circ = {}^\circ y$. $q_i$ is the $i$th component of the velocity vector [27–29].

$$\rho_{lPCM}\frac{\partial q_i}{\partial t} + \rho_{lPCM}\frac{\partial q_j q_i}{\partial x_j} = -\frac{\partial p}{\partial x_i} + \mu_{lPCM}\frac{\partial}{\partial x_j}\left(\frac{\partial q_i}{\partial x_j}\right) + (\rho\beta)_{lPCM} g_i (T - T_{mel}) + F(T) q_i \tag{2}$$

in which,

$$g_i = \begin{cases} 0i = 1 \\ gi = 2 \end{cases} \tag{3}$$

$$F(T) = A^* \frac{(\Omega - 1)^2}{0.001 + \Omega^3},$$
$$\Omega(T) = \{ \quad 0T \le T_{mel} - 0.5\delta T_{mel} \quad 0.5 - \frac{T_{mel} - T}{\delta T_{mel}} T_{mel} - 0.5\delta T_{mel} < T < T_{mel} + 0.5\delta T_{mel} \quad 1T \ge T_{mel} + 0.5\delta T_{mel} \tag{4}$$

$$(\rho c_p)_{PCM}\frac{\partial T}{\partial t} + (\rho c_p)_{PCM}\frac{\partial q_i T}{\partial x_i} = \frac{\partial}{\partial x_i}\left(k_{PCM}\frac{\partial T}{\partial x_i}\right) - \rho_{sPCM} h_{PCM}\frac{\partial \Omega(T)}{\partial t} \tag{5}$$

$$(\rho c_p)_{PCM} = \Omega(T)\left[(\rho c_p)_{lPCM} - (\rho c_p)_{sPCM}\right] + (\rho c_p)_{sPCM} \tag{6}$$

$$k_{PCM} = \Omega(T)[k_{lPCM} - k_{sPCM}] + k_{sPCM} \tag{7}$$

The following boundary and initial conditions are applied:
On the hot surfaces:

$$T = T_h = 320.15K, q_i = 0 \tag{8}$$

On the insulated vertical surfaces:

$$\frac{\partial T}{\partial x} = 0, q_i = 0 \tag{9}$$

On the insulated horizontal surfaces:

$$\frac{\partial T}{\partial y} = 0, q_i = 0 \tag{10}$$

Initial conditions:

$$T = T_{initial} = 300.15K, q_i = 0 \tag{11}$$

It is worth noting that this specified value is sufficiently lower than the melting temperature (melting temperature is 310.15 K). Moreover, this temperature is close enough to the ambient temperature (i.e., 298.15 K).

The melted volume fraction (*MVF*) of the PCM is:

$$MVF = \frac{A_{lPCM}}{A_{lPCM} + A_{sPCM}} \tag{12}$$

$A_{lPCM}$ and $A_{sPCM}$ are the liquid and solid surface areas of the PCM. At last, the equation for the stream function is introduced as follows:

$$\frac{\partial^2 \psi}{\partial x^2} + \frac{\partial^2 \psi}{\partial y^2} = \frac{\partial q_1}{\partial y} - \frac{\partial q_2}{\partial x} \tag{13}$$

where $q_1$ and $q_2$ represent the components of velocity vector in the $x$ and $y$ directions, respectively.

## 3. Numerical approach, mesh and time step sensitivity analyses, and code verification

### 3.1. Numerical approach

In this research, the enthalpy-porosity method has been employed for numerical modeling. For the examination of drastic changes in variables within the mushy zone, we utilized an adaptive mesh refinement to produce a grid of superior quality in the mushy zone. For discretization of nonlinear differential equations and the integration of user-defined codes, the capabilities of COMSOL Multiphysics software were used. Specifically, we implemented the Galerkin finite element method to effectively solve the governing equations [30]. This method initially divides the target domain into a series of smaller domains and then formulates a piecewise polynomial approximation of the solution over each of these smaller domains. The chosen method to discretize the domain for solving the momentum equations, and subsequently calculating the velocity and pressure variables, adopts a P1 + P1 discretization mode. This discretization mode denotes the use of linear elements for the velocity and pressure variables. In laminar flows, the default choice is P1 + P1. Opting for linear elements is advantageous as they are computationally more economical than their higher-order counterparts and generally result in fewer undesired oscillations, thereby enhancing numerical robustness. Additionally, when discretizing the energy equation for temperature calculation, a first-order, linear discretization method is employed [31]. In the Galerkin approach, the governing

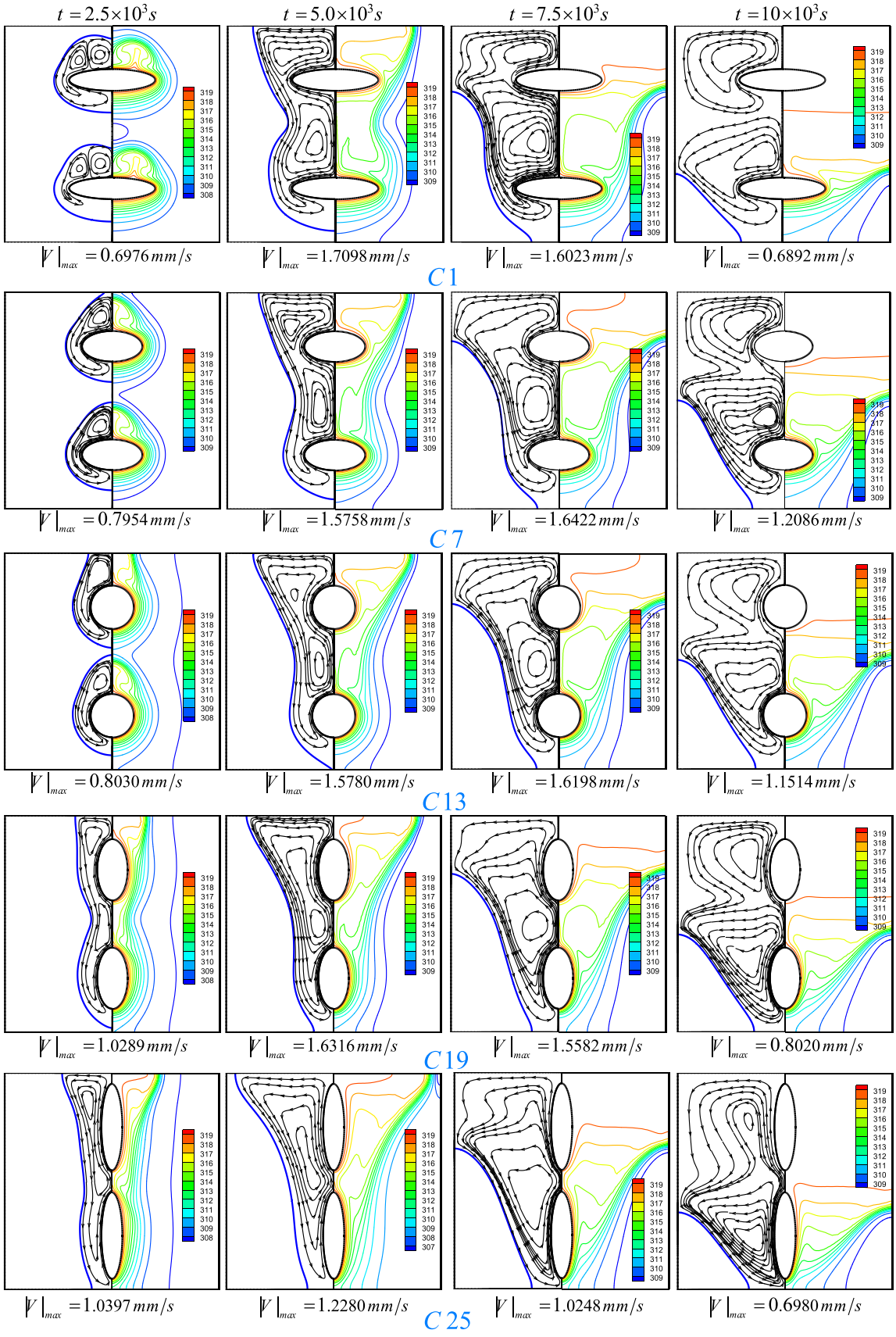


**Fig. 7.** Dependency of the melting fields, streamlines, and isotherms to the identical aspect ratios of the upper and lower elliptical cylinders.

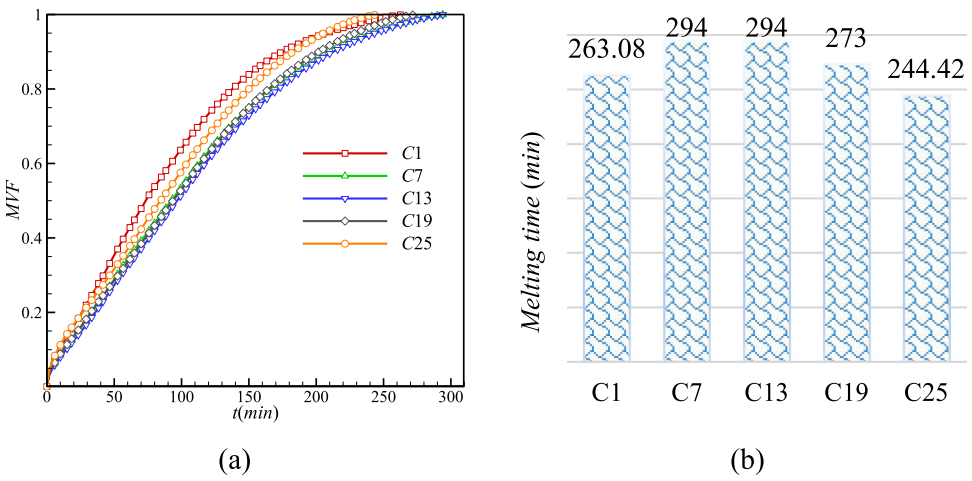


**Fig. 8.** Dependency of (a) the *MVF*, and (b) melting time to the identical aspect ratios of the upper and lower elliptical cylinders.

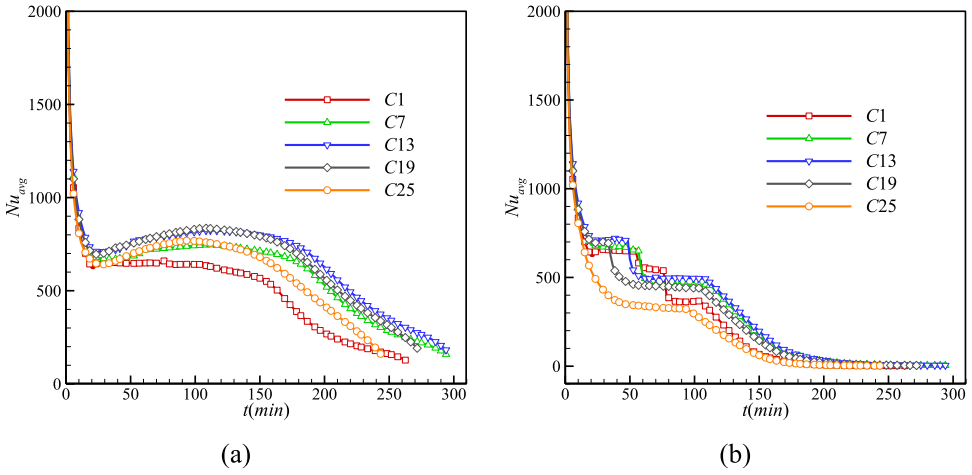


**Fig. 9.** Dependency of $Nu_{avg}$ of (a) the lower and (b) upper cylinders to the identical aspect ratios of the upper and lower elliptical cylinders.

equations are multiplied by a test function and integrated over the domain. The selection of the test function requires ensuring its orthogonality to the basis functions employed in the approximation. This choice guarantees that the resulting system of equations is well-posed and possesses a unique solution. The application of the Galerkin approach gives rise to a set of algebraic equations that can be solved through numerical methods using conventional techniques [32]. For resolving the residual equations, the PARallel DIrect SOlver is utilized, incorporating a Newtonian damping factor of 0.8 [33–35]. The iterations persist until meeting the residual error criterion of $10^{-5}$.

### 3.2. Mesh and time step sensitivity analyses

In the current numerical simulation, the mushy zone emerges as the most sensitive region to the grid. Therefore, an adaptive mesh refinement within the mushy region is used to reach the accuracy of a solution. Fig. 2 provides a visual representation of the progressive adaptive mesh at different times.

To achieve a balance between the precision and computational cost of the simulation process, grid sensitivity analysis is used in this investigation. As shown in Fig. 3, four levels of mesh fineness, are applied to discretize the model. The results show that a mesh with 8954 elements can be employed confidently for numerical calculations. Moreover, three distinct time steps are studied; $\Delta t = 0.8$ s, 0.4 s, and 0.1 s. The difference in *MVF* for $\Delta t = 0.4$ s and $\Delta t = 0.1$ s is virtually negligible, as depicted in Fig. 4. Consequently, to ensure accuracy and expedite computational processes, all numerical simulations in this work are executed with a fixed time step of $\Delta t = 0.4$ s

### 3.3. Code verification

The model developed in this study is validated using both the experimental and numerical results obtained by Kamkari et al. [36,37] for a rectangular enclosure filled with a PCM. In this verification, a rectangular enclosure with the size of 120 mm × 50 mm is filled by lauric acid as the PCM. A high temperature of $T_h = 70$ °C is applied to the right side of the enclosure, while the other walls are thermally insulated. As shown in Fig. 5, a good compatibility between the numerical outcomes of the current work and both the numerical and experimental findings reported in [36,37] can be found. Moreover, to enhance the confidence in the accuracy of the obtained results, the numerical values of *MVF* from this study undergo a quantitative comparison with the experimental and numerical data presented by Kamkari et al. [36,37]. The quantitative comparison depicted in Fig. 6 reveals that the results of the current study have a high level of accuracy.

## 4. Results and discussion

The cases under study are summarized in Table 2, classified according to the aspect ratio of the lower and upper elliptical cylinders. The volume of PCM filling the enclosure is constant, and the radii of the cylinders can be achieved by the aspect ratios. Obtained results

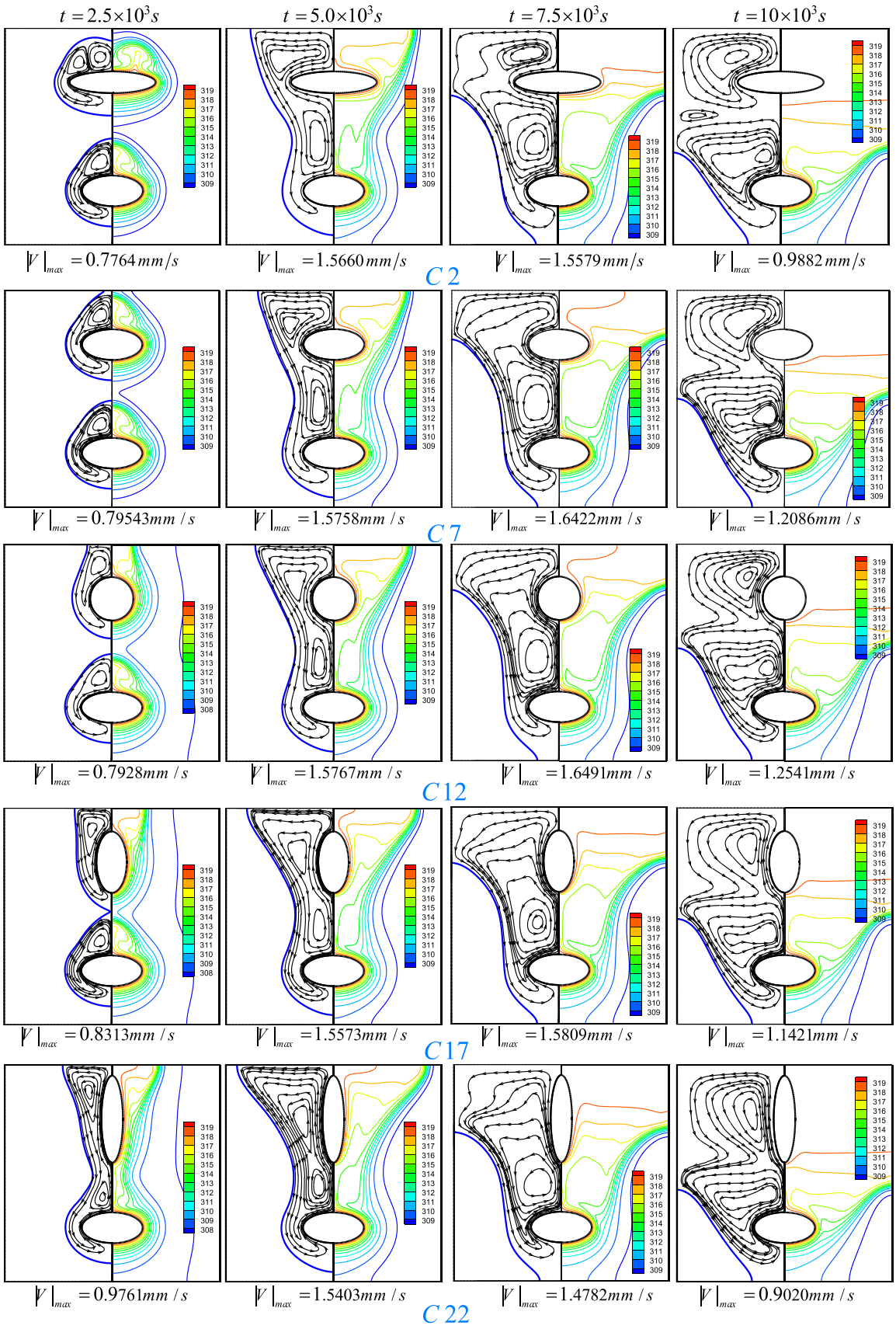


**Fig. 10.** Dependency of the melting fields, streamlines, and isotherms to the aspect ratio of the upper cylinder when $AR_l = 0.5$.

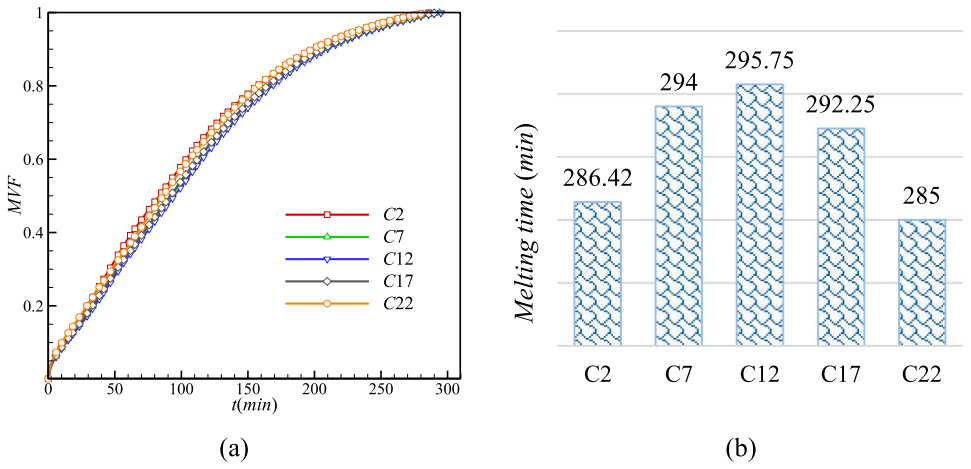


**Fig. 11.** Dependency of (a) the *MVF*, and (b) melting time to the aspect ratio of the upper elliptical cylinder when $AR_l = 0.5$.

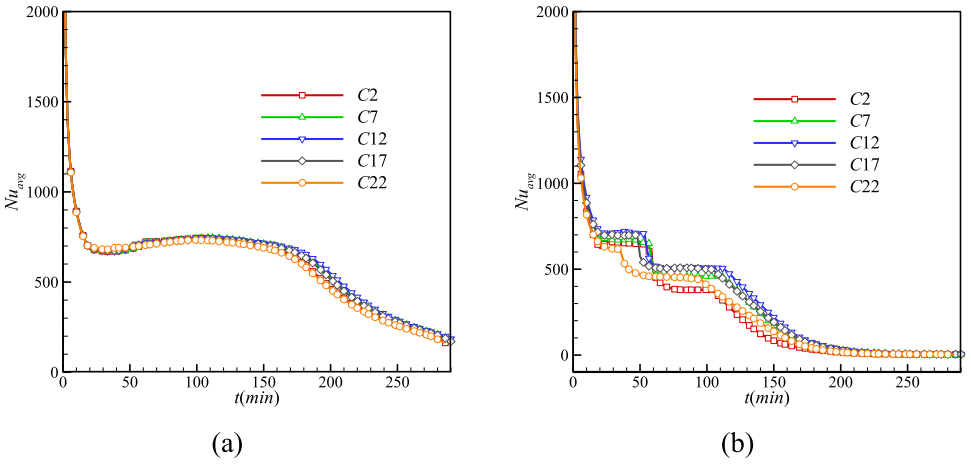


**Fig. 12.** Dependency of $Nu_{avg}$ of (a) the lower and (b) upper cylinders to the aspect ratio of the upper elliptical cylinder when $AR_l = 0.5$.

illustrating the streamlines, isotherms, melted volume fraction, melting or charging time, and average Nusselt numbers are presented in Figs. 7–16.

Fig. 7 shows the time evolution of streamlines and isotherms for different aspect ratios of internal cylinders with identical shapes. Here, the aspect ratios of the upper and lower cylinders are the same. It should be noted that the considered chargers (cylinders) are placed along the vertical middle cross-section. These cylinders are uniform, and their centers of inertia are located as shown in Fig. 1. For case *C*1 (see Table 2), the emergence of two thermal plumes above each cylinder can be observed at $t = 2500$ s and $t = 5000$ s. These thermal plumes combine, giving rise to ascending flows along the central vertical line of the cavity above each cylinder. It should be noted that initially, thermal plumes appear near the edges of the cylinders, influenced by the buoyancy force and the curved surfaces of the cylinders. Over time, these thermal plumes gradually move towards the central vertical axis, combining to form a unified thermal plume. As a result, at $t = 2500$ s, one can find thermal plumes located at the middle part of the mentioned distance, and at $t = 5000$ s, a single combined thermal plume is positioned along the vertical symmetry line. Moreover, at $t = 5000$ s, a combination of convective cells forms near the upper and bottom cylinders, creating a global circulation around these charges. This behavior can be attributed to the intense melting of PCM and the formation of convective liquid zones. Additionally, it is worth noting that at $t = 2500$ s, the melting zones near the bottom and upper cylinders are similar, attributed to the absence of interactions between these cylinders and between the thermal plume above the upper cylinder with the upper wall. While at $t = 5000$ s, a combination of these melting zones leads to the strong interaction between mentioned thermal plumes. For $t > 5000$ s, more intensive melting occurs in the upper part due to natural convection intensification with a huge melt volume. At $t = 10{,}000$ s, almost whole PCM is melted within the chamber. Solid PCM can be found only in the bottom corners of the enclosure due to intensive convective flow in the upper part and the dominance of heat conduction in the bottom zone.

Reducing the horizontal size and increasing the vertical size of the chargers (see case *C*7 in Table 2) result in the formation of a single thermal plume at $t = 2500$ s, accompanied by more intensive melting in the vertical direction. An appearance of a single thermal plume at $t = 2500$ s can be explained by less horizontal size of the charger compared to the previous case (*C*1). Further raise in time will not make charging effective like in previous case, i.e., *C*1. As a result, the charging time for *C*1 is significantly shorter compared to that observed in *C*7. It should be noted that the less horizontal sizes of the charges illustrate a less intensive melting of PCM within the chamber. In case *C*13, when we have circular inner cylinders, the PCM behavior is like case *C*7. Further vertical elongation of these chargers can be more effective considering more intensive natural convection along vertical plate compared to the horizontal ones. It is worth highlighting that an intensification of the charging process in the natural convection system can be described by the influence of buoyancy force. Therefore, the effect of vertical orientation of the cylinder on the melting process is similar to vertical plate

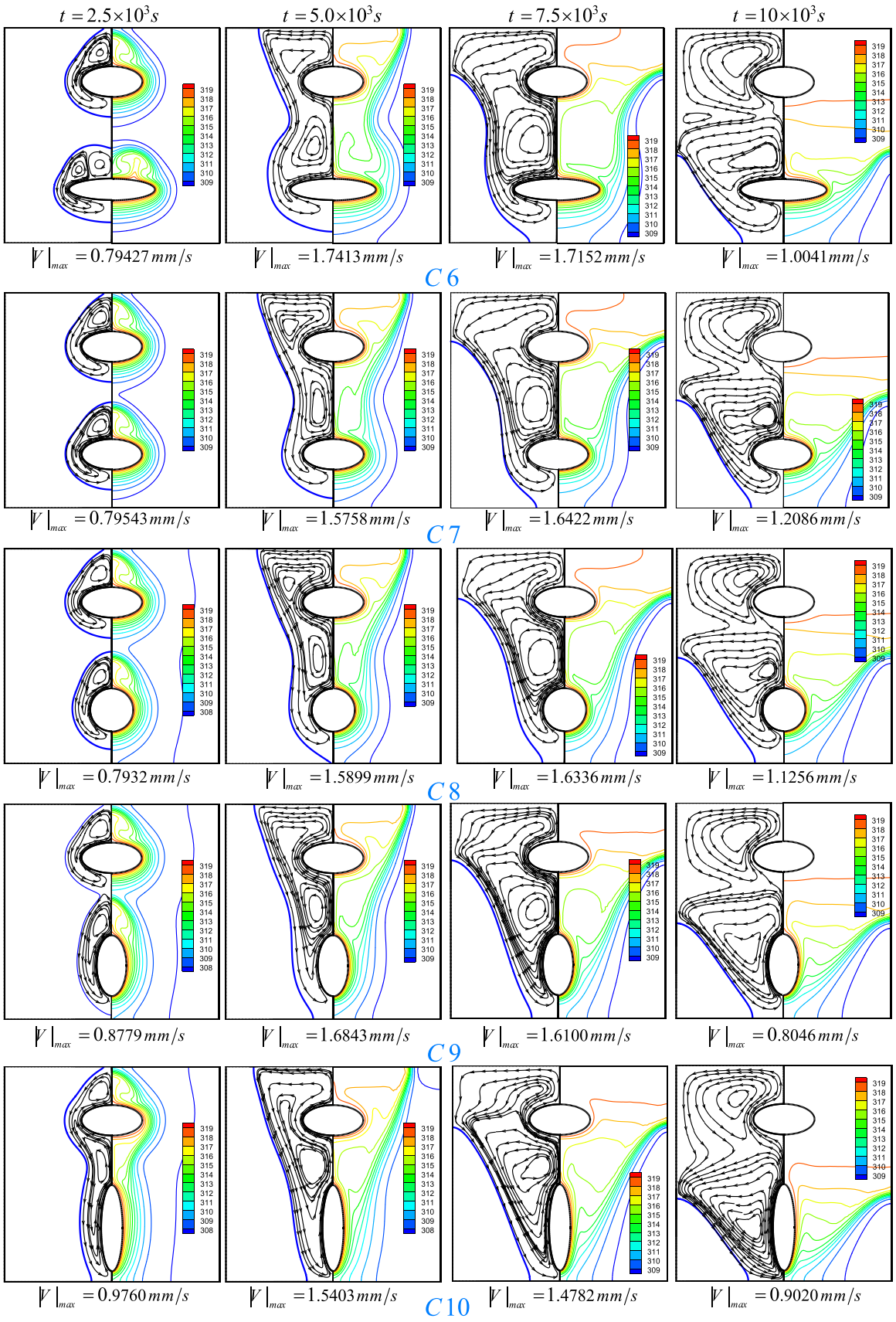


**Fig. 13.** Dependency of the melting fields, streamlines, and isotherms to the aspect ratio of the lower cylinder when $AR_u = 0.5$.

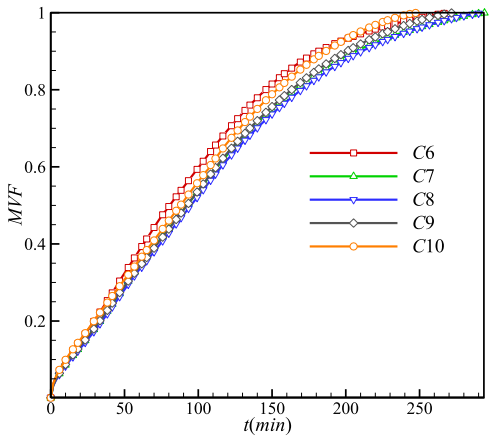


**Fig. 14.** Dependency of *MVF* to the aspect ratio of the lower elliptical cylinder when $AR_u = 0.5$.

and is more effective in comparison with horizontal orientation of the charger (cylinder) that is similar to horizontal plate. It is interesting to note that at $t = 2500$ s, only one global convective cell is formed, combining the bottom and upper circulations, in cases *C*19 and *C*25. This behavior can be attributed to the vertical elongation of the chargers, resembling the characteristics of vertical plates mentioned earlier. For the present problem, such a phenomenon can be explained by the rapid melting of the upper part for cases *C*19 and *C*25. Then, the melting process begins to heat the bottom solid material, and as a result, the melting time for these cases is lower compared to the previous ones. It is interesting to note that maximum convective flow velocity among the considered cases can be found for case *C*1 at $t = 5000$ s

Fig. 8 shows the time evolution of the *MVF* and charging/melting time for the considered cases. As shown, a more effective case is *C*25 when melting time is minimum, and consequently the charging process is most effective. It is interesting to note that in case *C*1, most of the melting process occurs for $t < 200$ min, whereas for *C*25, melting intensification takes place for $t > 200$ min. This can be explained by the difference between the heated vertical and horizontal plates within the convectively circulating liquid. Less effective cases are *C*7 ($AR_l = AR_u = 0.5$) and *C*13 ($AR_l = AR_u = 1.0$), each having a melting time of 294 min. Case *C*25, with $AR_l = AR_u = 4.0$, demonstrates a 16.86 % reduction in the melting time compared to the case *C*13. Furthermore, these reductions in the melting time are 10.52 % and 7.14 % for cases *C*1 ($AR_l = AR_u = 0.25$) and *C*19 ($AR_l = AR_u = 2.0$), respectively. It should be noted that less and more effective cases can be interchangeable, as they depend on the considered physical problem. Sometimes the objective is to decrease the charging time, e.g., for the LHTES system. However, in the case of cooling electronic devices or maintaining the working thermal mode, it is necessary to increase the melting time. Therefore, these considered cases can be optimal for different thermal systems.

Average Nusselt numbers behavior with time are shown in Fig. 9 for bottom and top cylinders. More effective cases with low charging time are characterized by low average Nusselt number for the upper and lower chargers due to the necessity of heating the material near the heater surfaces and vice versa. Taking into account that the upper cylinder is placed in the trail of velocity and temperature fields of the bottom charger, the average Nusselt number for the upper cylinder follows a decreasing trend over time. It is evident from Fig. 9 that the average Nusselt number of the bottom cylinder is a non-monotonic function of time. This behavior is attributed to the formation of the initial heat-conduction level and the development of natural convection heat transfer level. Furthermore, the minimum value of the average Nusselt number of the lower cylinder characterized a transition between these two mentioned levels.

Fig. 10 demonstrates the impact of the upper charger shape with $AR_l = 0.5$ on the streamlines and isotherms within the enclosure. The flow structure and temperature field near the upper and lower cylinders can be considered a combination of the cases described in Fig. 7. Adding cylinders of various shapes allows to control the flow structure and temperature field due to different impact of buoyancy force. Therefore, the inclusion of a horizontally oriented upper heater (case *C*2) reflects a higher necessity for melting of the upper part and the melting time for the considered chamber is lower compared to that of case *C*7. Vertically oriented upper heater allows to intensify melting phenomenon due to huge heating surface along the vertical coordinate. Considering the present analysis, the maximum convection velocity is 1.6491 mm/s for case *C*12 due to the circular shape of the upper cylinder. It is necessary to highlight that intensive melting of the upper part characterizes less melting time for the whole chamber. Consequently, cases *C*2 and *C*22 can be more effective from this point of view.

Fig. 11 presents the evolution of the *MVF* and melting time for different cases with $AR_l = 0.5$. It is clear that 300 min is enough for complete charging of the analyzed system. More intensive charging occurs for case *C*22 with a vertically elongated upper heater ($AR_u = 4.0$), while less intensive charging happens for case *C*12 with circular shape of the upper heater ($AR_u = 1.0$). The melting time difference between cases *C*12 and *C*22 is 10.75 min. As shown, deviation from $AR_u = 1.0$ leads to a decrease in the melting time. The percentage of melting time reduction for cases *C*2 ($AR_u = 0.25$), *C*7 ($AR_u = 0.5$), *C*17 ($AR_u = 2.0$), and *C*22 ($AR_u = 4.0$) compared to case *C*12 ($AR_u = 1.0$) is 3.20 %, 0.06 %, 1.18 %, and 3.60 %, respectively. The evolution of the average Nusselt numbers

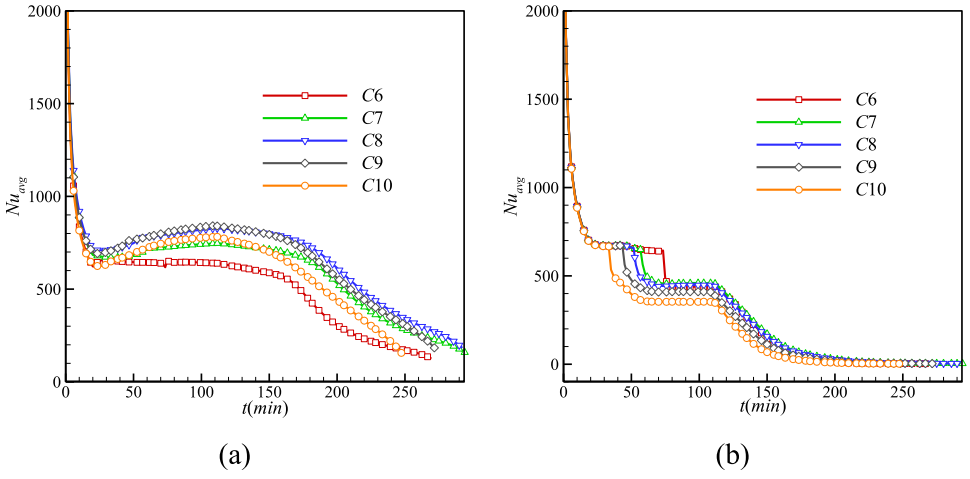


**Fig. 15.** Dependency of $Nu_{avg}$ of (a) the lower and (b) upper cylinders to the aspect ratio of the lower elliptical cylinder when $AR_u = 0.5$.

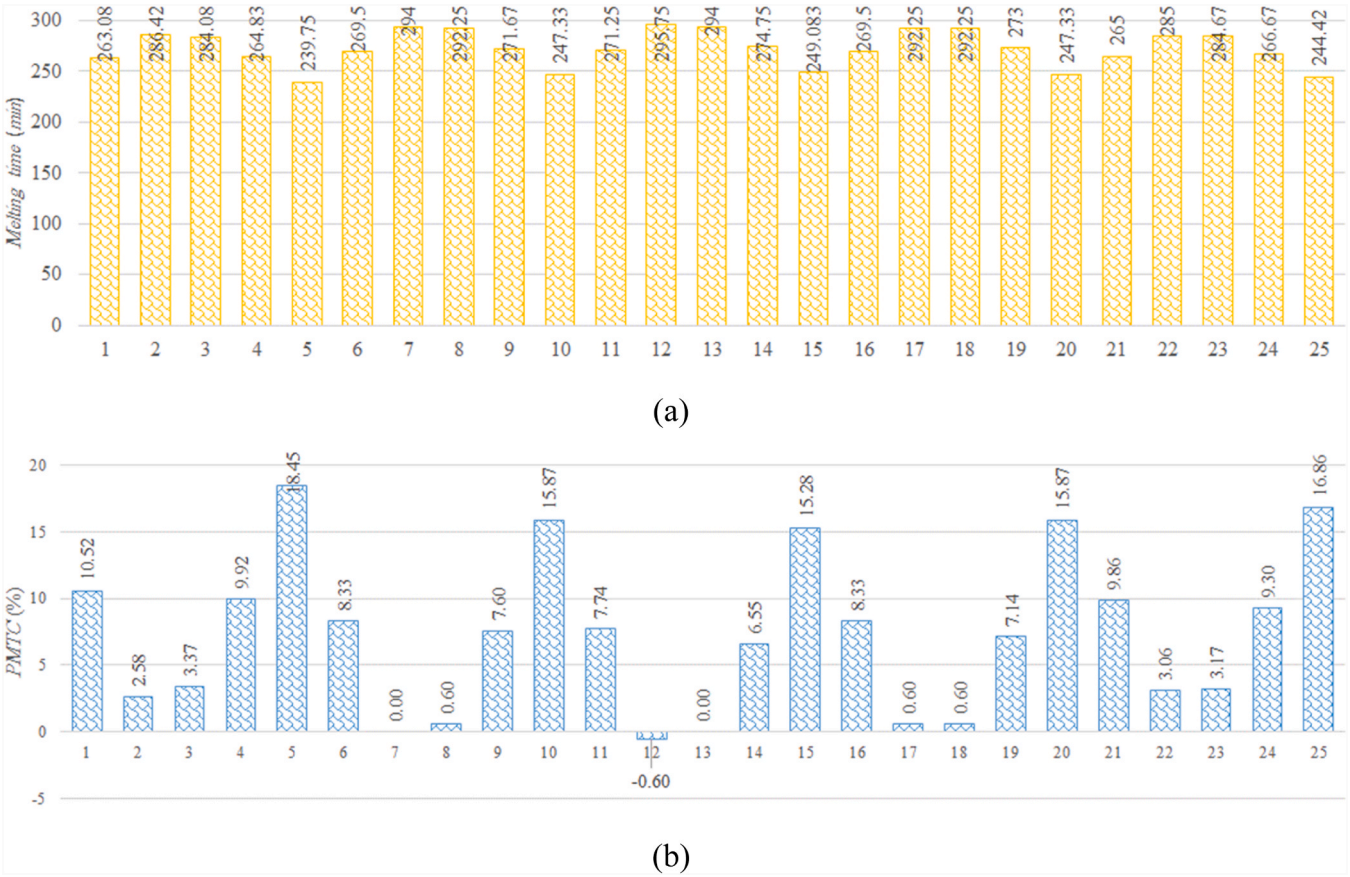


**Fig. 16.** (a) Melting time for the different cases, and (b) percentage of a decrease (positive) or an increase (negative) of the melting time compared to case *C*13 ($AR_l = AR_u = 1.0$).

for these heaters is shown in Fig. 12. It is worth noting that by keeping the bottom cylinder unchanged and changing the upper one, the average Nusselt number of the lower cylinder can vary with the variation of the upper cylinder shape. Behavior of the average Nusselt number has been extensively described earlier in Fig. 9 and for the considered cases, the nature of the average Nusselt number is similar. However, it is interesting to highlight that at $t = 300$ min, $Nu_{avg}$ for the upper heater reaches zero due to complete melting and significant heating of the upper part, while $Nu_{avg}$ for the lower heater is not equal to zero due to convective flow evolution and mixing between hot and less hot flows. Therefore, the thermal relaxation time for the considered system is greater than the whole melting time due to the natural convection phenomenon.

The streamlines and isotherms within the chamber for different shapes of the bottom heater are shown in Fig. 13 at $AR_u = 0.5$. Taking into account that the upper heater is placed in the flow and thermal trace of the bottom cylinder, it can be inferred that altering the shape of the lower heater can change the flow structure and temperature field of the entire system. Such features could be found in Fig. 13 compared to Fig. 7. The behavior of PCM was described previously in Figs. 7 and 10. Here, analyzing Fig. 14 shows that more intensive charging occurs for case *C*10 with vertical orientation of the bottom heater. In contrast, less intensive melting is observed for cases *C*7 and *C*8, where the shape of the bottom cylinder is nearly circular ($AR_l = 0.5$ and $AR_l = 1.0$).

The trend of the average Nusselt numbers presented in Fig. 15 aligns with what has been described in Figs. 9 and 12. As mentioned earlier, by changing the shape of the lower heater, it is found that the average Nusselt number for the upper cylinder can be more sensitive to such changes compared to the average Nusselt number of the lower heater. This is mainly due to the influence of the buoyancy force and, consequently, due to the interaction between the thermal plume formed above the bottom cylinder with the upper charger.

A more in-depth analysis shall be performed using the PMTC parameter, which defines the percentage of a decrease or increase in the melting time, as presented in Eq. (14).

$$PMTC(\%) = \frac{t|_{C13} - t|_{Ci}}{t|_{C13}} \times 100 \tag{14}$$

*i* in the above equation denotes the case number. It is worth noting that both the upper and lower cylinders of case *C*13 are circular. Indeed, the *PMTC* parameter indicates the percentage of decrease or increase in the melting time of different cases relative to the chamber with two circular cylinders. The melting time for the considered cases is shown in Fig. 16a. Here, the lowest value is 239.75 min for case *C*5, while the highest melting time is calculated as 295.75 min for case *C*12. Fig. 16b shows *PMTC* behavior for different cases. This graph helps to strengthen the findings presented in Fig. 16a. This figure shows that case *C*5 ($AR_l$ =4.0 and $AR_u = 0.25$) has the highest percentage of a decrease in the melting time ($PMTC = 18.45$ %), while case *C*12 ($AR_l$ =0.5 and $AR_u = 1.0$) has a negative percentage compared with other cases ($PMTC = -0.60$ %). It is worth noting that the negative value of *PMTC* shows an increase in the melting time of the system compared to case *C*13 ($AR_l = AR_u = 1.0$).

## 5. Conclusions

Numerical analysis of the phase change material charging within the adiabatic square chamber with two isothermal heaters has been performed using finite element technique. To model the mushy zone with

high accuracy, an adaptive mesh refinement has been employed. The developed computational code has been validated against numerical and experimental data from the literature. In addition, analysis of the effect of heater's shape on the flow structure, melting fields, and heat transfer mode has been conducted. The findings of this study can be summarized below:

1. Flow structure and heat transfer within the considered chamber are defined mainly by the shape of the bottom heater.
2. The average Nusselt number of the upper and lower cylinders depend significantly on the aspect ratio. Such behavior can be explained by essential impact of buoyancy force.
3. The thermal relaxation time for the considered system is greater than the whole melting time due to the natural convection phenomenon.
4. More intensive charging of the considered systems occurs in case $C5$ with $AR_l = 4.0$ and $AR_u = 0.25$ (melting time is 239.75 min), while less intensive charging happens in case $C12$ with $AR_l = 0.5$ and $AR_u = 1.0$ (melting time is 295.75). In comparison to the case with $AR_u = AR_l = 1.0$, the percentage of the decrease and increase in the melting time for cases $C5$ and $C12$ is 18.45 % and 0.6 %, respectively.
5. Compared to the case with $AR_u = AR_l = 1.0$, the case with $AR_l = AR_u = 4.0$, exhibits a notable 16.86 % reduction in the melting time. Moreover, these reductions in the melting time are 10.52 % and 7.14 % for cases with $AR_l = AR_u = 0.25$ and $AR_l = AR_u = 2.0$, respectively. It is worth noting that the melting times of the cases with $AR_l = AR_u = 0.5$ and $AR_u = AR_l = 1.0$ are the same.
6. In the system with $AR_l = 0.5$, changing the shape of the upper cylinder from circular ($AR_u = 1.0$) to elliptical ($AR_u \ddagger 1.0$) leads to a reduction in the melting time. The percentage of melting time reduction for cases with aspect ratio ($AR_u$) values of 0.25, 0.5, 2.0, and 4.0, compared to the case with $AR_u = 1.0$, is 3.20 %, 0.06 %, 1.18 %, and 3.60 %, respectively.
7. It should be noted that more intensive charging can be more effective for various engineering systems, while less intensive melting is not so effective and vice versa. This trend depends on the considered physical or technical problem. Sometimes the objective is to reduce the charging time, e.g., for the latent thermal energy storage system, however in the case of cooling electronic devices or maintaining the working thermal mode, it is necessary to increase the melting time. Therefore, the considered cases in the present study can be optimal for different thermal systems.

## Declaration of Competing Interest

The authors declare that they have no conflict of interest.

## Acknowledgments

This study is supported via funding from Prince Sattam bin Abdulaziz University project number (PSAU/2023/R/1444).

## References

[1] M. Shahabadi, B. Alshuraiaan, A. Abidi, O. Younis, M. Ghalambaz, S. Mehryan, Transient melting flow of a NePCM comprising GNPs in a semi-elliptical latent heat thermal energy storage unit, Int. Commun. Heat. Mass Transf. 130 (2022), 105815.
[2] H. Nazir, M. Batool, F.J.B. Osorio, M. Isaza-Ruiz, X. Xu, K. Vignarooban, P. Phelan, A.M. Kannan, Recent developments in phase change materials for energy storage applications: a review, Int. J. Heat. Mass Transf. 129 (2019) 491–523.
[3] A. Hussain, S.M. Arif, M. Aslam, Emerging renewable and sustainable energy technologies: state of the art, Renew. Sustain. Energy Rev. 71 (2017) 12–28.
[4] D. Chiappini, A coupled lattice Boltzmann-finite volume method for phase change material analysis, Int. J. Therm. Sci. 164 (2021), 106893.
[5] J.P. Da Cunha, P. Eames, Thermal energy storage for low and medium temperature applications using phase change materials–a review, Appl. Energy 177 (2016) 227–238.
[6] S. Hosseinizadeh, A.R. Darzi, F. Tan, Numerical investigations of unconstrained melting of nano-enhanced phase change material (NEPCM) inside a spherical container, Int. J. Therm. Sci. 51 (2012) 77–83.
[7] W.-B. Ye, M. Arıcı, Redefined interface error, 2D verification and validation for pure solid-gallium phase change modeling by enthalpy-porosity methodology, Int. Commun. Heat. Mass Transf. 147 (2023), 106952, https://doi.org/10.1016/j.icheatmasstransfer.2023.106952.
[8] S. Ghani, E.M.A.A. ElBialy, F. Bakochristou, S.M.A. Gamaledin, M.M. Rashwan, The effect of forced convection and PCM on helmets' thermal performance in hot and arid environments, Appl. Therm. Eng. 111 (2017) 624–637.
[9] A.A. Al-Abidi, S.B. Mat, K. Sopian, M. Sulaiman, C. Lim, A. Th, Review of thermal energy storage for air conditioning systems, Renew. Sustain. Energy Rev. 16 (8) (2012) 5802–5819.
[10] W.-B. Ye, M. Arıcı, False diffusion, asymmetrical interface, and equilibrious state for pure solid-gallium phase change modeling by enthalpy-porosity methodology, Int. Commun. Heat. Mass Transf. 144 (2023), 106746, https://doi.org/10.1016/j.icheatmasstransfer.2023.106746.
[11] W.A. Dukhan, N.S. Dhaidan, T.A. Al-Hattab, F.N. Al-Mousawi, Phase-change of paraffin inside heat exchangers: an experimental study, Int. J. Environ. Sci. Technol. 19 (4) (2022) 3155–3164, https://doi.org/10.1007/s13762-021-03367-2.
[12] N.S. Dhaidan, Thermal performance of constrained melting of PCM inside an elliptical capsule of two orientations, Iran. J. Sci. Technol. Trans. Mech. Eng. 45 (2) (2021) 515–521, https://doi.org/10.1007/s40997-020-00345-w.
[13] P. Huang, G. Wei, L. Cui, G. Wang, X. Du, A morphology optimization of enclosure shape of low melting point alloy-based PCM heat sink, J. Energy Storage 64 (2023), 107153, https://doi.org/10.1016/j.est.2023.107153.
[14] R. Mukhesh, K.P. Sarath, M. Feroz Osman, M. Deepu, K.V. Manu, Asymmetric PCM melting and thermal convection in a rectangular enclosure with straight and wavy heat transfer passages, Int. J. Heat. Mass Transf. 217 (2023), 124625, https://doi.org/10.1016/j.ijheatmasstransfer.2023.124625.
[15] A.A. Al-Abidi, S.B. Mat, K. Sopian, M. Sulaiman, A.T. Mohammed, CFD applications for latent heat thermal energy storage: a review, Renew. Sustain. Energy Rev. 20 (2013) 353–363.
[16] L. Zeng, J. Lu, Y. Li, W. Li, S. Liu, J. Zhu, Numerical study of the influences of geometry orientation on phase change material's melting process, Adv. Mech. Eng. 9 (10) (2017), 1687814017720084.
[17] W.-B. Ye, M. Arıcı, 3D validation, 2D feasibility, corrected and developed correlations for pure solid-gallium phase change modeling by enthalpy-porosity methodology, Int. Commun. Heat. Mass Transf. 144 (2023), 106780, https://doi.org/10.1016/j.icheatmasstransfer.2023.106780.
[18] A.O. Elsayed, Numerical investigation on PCM melting in triangular cylinders, Alex. Eng. J. 57 (4) (2018) 2819–2828.
[19] A.M. Soodmand, S. Nejatbakhsh, H. Pourpasha, H. Aghdasinia, S.Z. Heris, Simulation of melting and solidification process of polyethylene glycol 1500 as a PCM in rectangular, triangular, and cylindrical enclosures, Alex. Eng. J. 61 (11) (2022) 8431–8456, https://doi.org/10.1016/j.aej.2022.02.011.
[20] N.S. Dhaidan, A.F. Khalaf, J.M. Khodadadi, Numerical and experimental investigation of melting of paraffin in a hemicylindrical capsule, J. Therm. Sci. Eng. Appl. 13 (5) (2021), https://doi.org/10.1115/1.4049873.
[21] A. Memon, G. Mishra, A.K. Gupta, Buoyancy-driven melting and heat transfer around a horizontal cylinder in square enclosure filled with phase change material, Appl. Therm. Eng. 181 (2020), 115990.
[22] M. Sugawara, Y. Komatsu, H. Beer, Melting and freezing around a horizontal cylinder placed in a square cavity, Heat. Mass Transf. 45 (1) (2008) 83–92.
[23] K. Sasaguchi, K. Kusano, R. Viskanta, A numerical analysis of solid-liquid phase change heat transfer around a single and two horizontal, vertically spaced cylinders in a rectangular cavity, Int. J. Heat. Mass Transf. 40 (6) (1997) 1343–1354.
[24] M. Mahdaoui, T. Kousksou, S. Blancher, A.A. Msaad, T. El Rhafiki, M. Mouqallid, A numerical analysis of solid–liquid phase change heat transfer around a horizontal cylinder, Appl. Math. Model. 38 (3) (2014) 1101–1110.
[25] G. Mishra, A. Memon, A.K. Gupta, N. Nirmalkar, Computational study on effect of enclosure shapes on melting characteristics of phase change material around a heated cylinder, Case Stud. Therm. Eng. 34 (2022), 102032.
[26] Z.-Q. Zhu, M.-J. Liu, N. Hu, Y.-K. Huang, L.-W. Fan, Z.-T. Yu, J. Ge, Inward solidification heat transfer of nano-enhanced phase change materials in a spherical capsule: an experimental study, J. Heat. Transf. 140 (2) (2018).
[27] H.F. Oztop, Natural convection in partially cooled and inclined porous rectangular enclosures, Int. J. Therm. Sci. 46 (2) (2007) 149–156.
[28] M. Ghalambaz, S.A.M. Mehryan, A. Hajjar, O. Younis, M.A. Sheremet, M.S. Pour, C. Hulme-Smith, Phase-transition thermal charging of a channel-shape thermal energy storage unit: taguchi optimization approach and copper foam inserts, Molecules 26 (5) (2021) 1235.
[29] N.S. Bondareva, B. Buonomo, O. Manca, M.A. Sheremet, Heat transfer performance of the finned nano-enhanced phase change material system under the inclination influence, Int. J. Heat. Mass Transf. 135 (2019) 1063–1072.
[30] R.L. Taylor, O.C. Zienkiewicz, The Finite Element Method, Butterworth-Heinemann Oxford, 2013.
[31] M. Dash, Blood Flow Dynamics on a Centrifugally Actuated Microfluidic Platform, Interdisciplinary, Indian Institute of Technology, Kharagpur, 2014, p. 48.
[32] Author Biography, in:O.C. Zienkiewicz, R.L. Taylor, P. Nithiarasu (Eds.), The Finite Element Method for Fluid Dynamics, Seventh edition.,, Butterworth-Heinemann, Oxford, 2014, p. ii. Author Biography, in:.
[33] O. Schenk, K. Gärtner, Solving unsymmetric sparse systems of linear equations with PARDISO, Future Gener. Comput. Syst. 20 (3) (2004) 475–487.
[34] P. Wriggers, Nonlinear Finite Element Methods, Springer Science & Business Media, 2008.

[35] F. Verbosio, A. De Coninck, D. Kourounis, O. Schenk, Enhancing the scalability of selected inversion factorization algorithms in genomic prediction, J. Comput. Sci. 22 (2017) 99–108.
[36] B. Kamkari, H. Shokouhmand, F. Bruno, Experimental investigation of the effect of inclination angle on convection-driven melting of phase change material in a rectangular enclosure, Int. J. Heat. Mass Transf. 72 (2014) 186–200.
[37] B. Kamkari, H.J. Amlashi, Numerical simulation and experimental verification of constrained melting of phase change material in inclined rectangular enclosures, Int. Commun. Heat. Mass Transf. 88 (2017) 211–219, https://doi.org/10.1016/j.icheatmasstransfer.2017.07.023.